MOUNT HOLYOKE COLLEGE

The effect of oxygen vacancies on proton conduction in 12.5% Sc-doped $BaZrO_3$

by

Ziqing Lin

A thesis submitted in partial fulfillment for the degree of Bachelor of arts

in the

Maria Alexandra Gomez Group
Chemistry

June 2020

Declaration of Authorship

I, Ziqing LIN, declare that this thesis titled, 'THE EFFECT OF OXYGEN VACANCIES ON PROTON CONDUCTION IN 12.5% AL, SC, AND Y-DOPED $BAZRO_3$' and the work presented in it are my own. I confirm that:

- This work was done wholly or mainly while in candidature for a research degree at this University.
- Where any part of this thesis has previously been submitted for a degree or any other qualification at this University or any other institution, this has been clearly stated.
- Where I have consulted the published work of others, this is always clearly attributed.
- Where I have quoted from the work of others, the source is always given. With the exception of such quotations, this thesis is entirely my own work.
- I have acknowledged all main sources of help.
- Where the thesis is based on work done by myself jointly with others, I have made clear exactly what was done by others and what I have contributed myself.

Signed:

_____

Date:

_____

MOUNT HOLYOKE COLLEGE

Abstract

Maria Alexandra Gomez Group

Chemistry

Degree of bachelor of arts

by Ziqing Lin

Fuel cells avoid the combustion process and hence are both more efficient and environmentally friendly than the common practice of burning fuels at power plants. Y-doped barium zirconium oxide ($BaZrO_3$) represents one of the most promising materials for stationary hydrogen fuel cells due to its ability to conduct hydrogen ions (protons)[1, 2]. Recently, it is found that Sc-doped $BaZrO_3$ has exhibited comparable proton conductivity as Y-doped ($BaZrO_3$)[3]. However, the introduction of the less positive dopant defects Sc^{3+} and Y^{3+} at the Zr^{4+} site, leads to the formation of proton traps. Inspired by studies suggesting that oxygen vacancies decrease trapping near dopant defects, this study aims to understand the effect of an oxygen vacancy on the minimum energy pathways, proton traps, and overall proton conduction in 12.5% Sc doped $BaZrO_3$ Perovskite[4]. Density functional theory (DFT) with the PBE functional in the Vienna ab-initio simulation package (VASP)[5] was used to find the total electronic energy for perovskite configurations. The conjugate-gradient minimization method is used to find the lowest energy structures for doped barium zirconium oxide systems starting from the 23 possible Glazer[6] distortions. The Nudged Elastic Band (NEB) method was used to find activation barriers for oxygen vacancy motion. The influence of a dopant nearest neighbor oxygen vacancy on the proton energy landscape was determined by finding the relative energies for chemically distinct proton binding sites as well as transition states between sites close and far from the oxygen vacancy. Finally, Kinetic Monte Carlo (KMC) simulation is used to find the most abundant limiting barrier and explore the proton conduction trajectory.

Acknowledgements

I would like to express my deepest gratitude towards everyone who have offer me tremendous help and support not only in completing this thesis, but also in moving forward to pursue a higher education in chemistry. I would like to thank professor Gomez for the guidance she offered during every stage of the process. Without her foresight to start things ahead of time, I am afraid things would be completely different. I am grateful to every member, Shiyun Lin, Jiayun Zhong, and Megha Patel in the Gomez's group who makes Carr G18 feel like home. I would like to thank my advisor professor Ashby for the infinite helpful advice, mental support, and cookies. I am grateful to my thesis committee members, Alan van Giessen and Spencer Smith. Finally, I would like to thank all the professors in the chemistry department for the amazing four years.

The computational and financial support provided by MERCURY, Mount Holyoke college, and the National Science Foundation is gratefully acknowledged.

Contents

List of Figures

List of Tables

Abbreviations

DFT	**D**ensity **F**unctional **T**heory
GGA	**G**eneralized **G**radient **A**pproximation
KMC	**K**inetic **M**onte **C**arlo
LDA	**L**ocal **D**ensity **A**pproximation
MEP	**M**inimum **E**nergy **P**ath
NEB	**N**udged **E**lastic **B**and
CNEB	**C**limbing **N**udged **E**lastic **B**and
PAW	**P**rojefctor **A**ugmented **W**ave
PBE	**P**erdew **B**ruke **E**rnzerhof
PES	**P**otential **E**nergy **S**urface
VASP	**V**ienna **A**b-initio **s**simulation **P**ackage

Symbols

E	Energy
$\widehat{H}$	Hamiltonian
$\widehat{T}$	Kinetic energy operator
V	Potential energy operator
Ψ	Wavefunction

Chapter 1

Introduction

Dwindling fossil fuel reserves and global warming has raised environmental awareness in the past few years leading people to start seeking alternative energy sources, like solar energy and fuel cells. Fuel cells, environmentally friendly alternatives that avoid the combustion process, have been rigorously studied. Hydrogen fuel cells show great promise in energy conversion with no harmful by-products. Among them, doped barium zirconium oxide ($BaZrO_3$) represents one of the most promising materials for stationary hydrogen fuel cells because of its ability to conduct protons. An experimental study suggested comparable proton conduction in Sc doped system in the presence of oxygen vacancy[8]. This study extends the previous work on perovskites [2, 9–11], aiming to find the minimum energy pathways, identify the locations where the protons are trapped, and determine the overall trajectory of proton conduction in Sc doped $BaZrO_3$ in the presence of an oxygen vacancy.

1.1 Doped perovskite as alternative energy source

The continual decrease of fossil fuel reserves and global environmental issue have encouraged people to turn their attention towards alternative energy sources, for instance, fuel cells. Fuel cell is an electrochemical cell that converts chemical energy of a fuel and oxidizing agent into electrical energy, without generating many pollutants. The overall reaction of fuel cell is shown below:

$$H_2 + \frac{1}{2}O_2 \rightarrow H_2O \tag{1.1}$$

is composed of an oxidation process at the anode:

$$H_2 \rightarrow 2H^+ + 2e^- \tag{1.2}$$

and the reduction reaction at the cathode where the exhaust gas is water:

$$\frac{1}{2}O_2 + 2e^- + 2H^+ \rightarrow H_2O \tag{1.3}$$

One of the most common types of fuel cells is hydrogen fuel cell. The hydrogen fuel cell is driven by the continual influx of oxygen ion that travel through an electrolyte from cathode to anode. Aiming to enhance electrical efficiency at reduced cost, it is necessary to find electrolyte material with higher proton conductivity. Perovskite oxides have shown great potential to be used as both the electrolyte and cathode in fuel cell. Among the perovskite oxides, $BaZrO_3$ has shown the highest bulk protonic conductivity along with high stability.

Additionally, the addition of dopant also influence the bulk proton conductivity. Previous research has shown that Y-doped $BaZrO_3$ has the highest proton mobility and consequently highest proton conductivity [1, 12]. Recently, it is found that Sc-doped $BaZrO_3$ has exhibit comparable proton conductivity as Y-doped $BaZrO_3$[8].

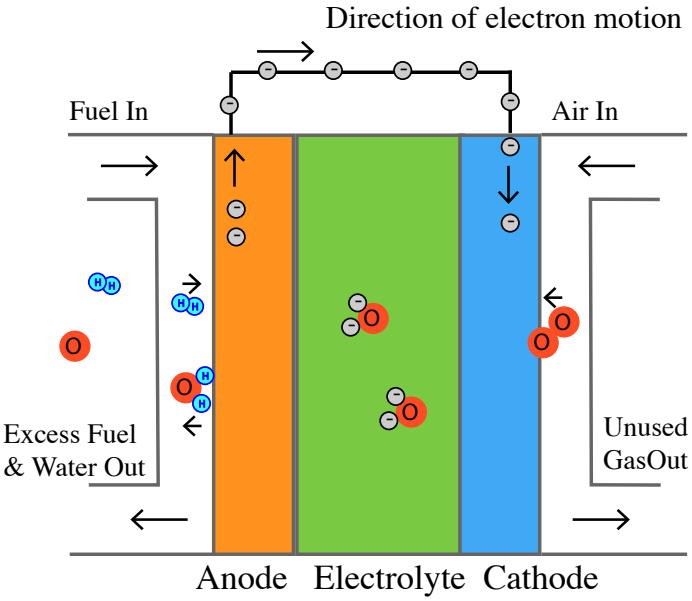

FIGURE 1.1: The schematic of a hydrogen fuel cell, with continual influx of oxygen gas that was reduced at the cathode, and the liberation of electrons at the anode.

Perovskite oxides have the general form of ABO_3 shown in Fig. 1.2(a). In the figure, there are two key packings in the basic perovskite structure namely the packing along the diagonal AOA, displayed as a black line, and the packing along the body centered line OBO, shown as a white line. When the radii of the ions involved is very compatible, the lattice size calculated from the diagonal packing and the body centered line packing is the same.

However, when a larger dopant ion is substituted at the B site, a deviation from the ideal structure appears, and the degree of deviation can be calculated by tolerance factor t, with r_A, r_B, r_O being the radii of the A, B, ane O ions.

$$t = \frac{r_A + r_B}{\sqrt{2}(r_B + r_o)} \tag{1.4}$$

The tolerance factor compares the lattice size obtained from perfect packing along the diagonal AOA line with the one from the body centered OBO line. An ideally cubic structure will have tolerance factor equals 1, which is roughly the case for barium zirconate. However, when the tolerance factor is not equal to 1, for instance, when a larger dopant is introduced at the B site, the body centered line OBO will lengthen, forcing the diagonal AOA line to lengthen even more to create extra space for the oxygen ions; thereby, leading to the octahedral arrangement of oxygen ions around the B sites as shown in Fig. 1(b). The tilting direction alternates on adjacent corner sharing octahedra bringing some oxygens closer together and others further apart leading to a greater diversity of oxygen types and hence a richer proton conduction energy landscape[2, 13].

1.2 Twenty three glazer structures

Because of octahedral tilting, the various layers of perovskite can distort into distinct configurations, giving rise to the need to categorize them. Glazer identified 23 possible octahedral distortions in a $2 \times 2 \times 2$ perovskite system[6]. The Glazer notations are used: + refers to subsequent layers tilting in the same directions, - in

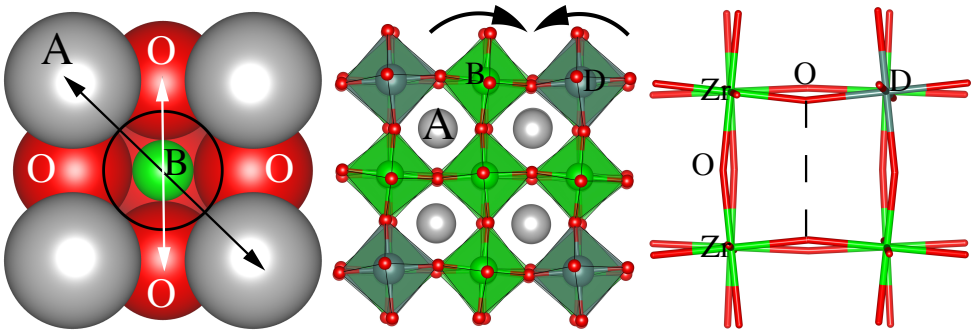

(a) (b) (c)

FIGURE 1.2: (a) shows the a basic ABO_3 perovskite unit cell in atomic size with a space filling model. Notice that the oxygen ions around the B ion form an octahedron. Four labeled oxygen ions are shown around the B ion, there is also an oxygen below the B ion. The front-most oxygen has been made transparent for clarity. (b) shows replicated perovskite unit cells in a polyhedral model highlighting octahedra around B ions and octahedra around dopant ions. The arrows above B and D octahedra indicate opposite direction tilting necessary for adjacent octahedra which are connected by oxygen corners (c) shows a stick model of upper right cube in (b), highlighting a case where subsequent layers of the perovskite have an opposite tilting scheme. In (c) a pair of oxygen ions in each face come closer together while another get further apart. The dashed line highlight the longer O...O oxygen ion pairs.

opposite directions, and 0 represent a perfectly cubic structure. Fig. 1(c) shows a - Glazer distortion perpendicular to the surface normal, with a pair of oxygen ions coming closer together while another one gets further apart in each plane. The distortion can also be different along the planes perpendicular to two other axes. The Glazer distortion label and the degree of distortion, measured by the ZrOZr and ZrOD angle distributions, describes the initial proton conduction landscape or network of oxygen ions[13].

1.3 Proton conductivity in Sc doped $BaZrO_3$ and proton trap

Proton can then migrate within the proton conduction network of oxygen ions, and the level of mobility can be influence by many factors, like temperature, or the introduction of dopant. Draber and *et al* have found that proton mobility is related to the concentration of dopant Y in $BaZrO_3$ system. At low concentration, a decrease in mobility appears. This is because as dopant concentration increase, there is a shift towards the right in the following equilibrium. The left hand side of the equation shows isolated dopant-proton pairs, while the right hand side shows that proton is trapped by dopant.

$$Y'_{Zr} + H_i^{\bullet} \longleftrightarrow \{Y'_{Zr} + H_i^{\bullet}\} \tag{1.5}$$

As the concentration of dopant pass a certain threshold, the proton mobility increase due to the formation of percolation pathway, and the structure with highest possible proton mobility has 12.5% dopant, which is the system explored in this study[12].

However, the introduction of the less positive dopant defects Al'_{Zr}, Sc'_{Zr} and Y'_{Zr} leads to the formation of proton trap (right hand side of Equation 1.5). As the substitution of Zr^{4+} with a less positive Y^{3+} decrease the repulsion for positive charged H^+ ;thereby, leading to the formation of proton trap, consequently

reducing proton mobility. It is also found that the size of the proton trap is correlated with the size of the dopant ion: smaller dopants like Al^{3+} has OH tilting to stabilize the proton binding site via hydrogen bonding; while larger dopant Y^{3+}, serve as a strong proton trap center that influence the mobility of protons in $BaZrO_3$[14].

Since former studies have explored the effect of Al and Y dopant on the proton conduction pathways on barium zirconate[2, 9–11]. and these two differently sized dopants show that Al'_{Zr} and Y'_{Zr} dopant defects shape the proton conduction landscape affecting proton conduction pathways, traps and key nexuses between trapped regions and proton conduction highways in significantly different ways. It is natural to understand how the size of dopant influences the proton conduction pathway. To fill in the missing puzzle between Al and Y system, this paper focuses on Sc dopant, which is larger than Al but smaller than Y. Also, experimental study suggests faster conduction in Sc doped system in the presence of oxygen vacancy.

.

1.4 Oxygen vacancy to counter proton trap

To hinder the formation of proton trap, oxygen vacancies can be added near the dopant defect to decrease attraction towards proton. Since both the oxygen vacancy and proton are positively charged, the repulsive interaction between like charges prevent the formation of proton trap. Studies have further found that in Sc doped $BaZrO_3$, the dopant-vacancy association $V_O^{\bullet\bullet}$-Sc can effectively suppress

formation of proton trap[4].

Oxygen vacancy can further alter the proton conduction landscape by inducing a tilting in the oxygen backbone, as shown in Kim's study[4]. Since different location of oxygen vacancy location shapes the proton conduction pathway differently, and as can be seen in Figs. 1.2(b) and (c), there are a number of oxygen sites and thus a number of possible vacancy locations, it is therefore necessary to categorize the oxygen sites. After considering all options in a $2 \times 2 \times 2$ unit cell perovskite system with one dopant ion, the 24 possible oxygen ion locations are categorized into three distinct sites based on symmetry. As shown in Fig. 1.3, the three types of oxygen ion sites at which a vacancy could be introduced are nearest, second nearest, and third nearest neighbors to a dopant defect, shown in decreasing shading of red. Nearest oxygen is the closest neighbor away from the dopant Sc, shown in the darkest red; second nearest oxygen is the second closest neighbor away, shown in red; third nearest oxygen is the third closest neighbor away shown in pink. Therefore, oxygen vacancy could be introduced at these three distinct sites.

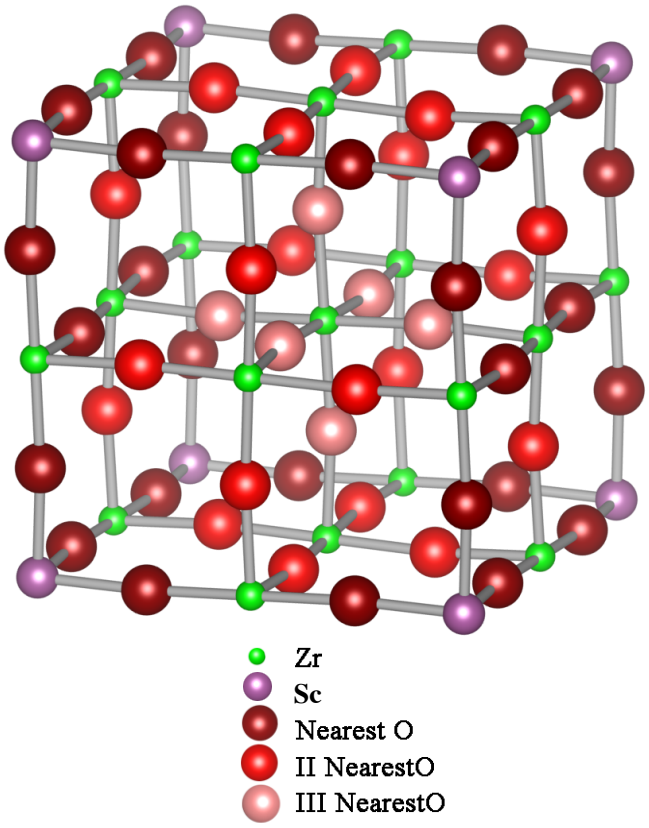

FIGURE 1.3: The general structure of a 12.5% yttrium doped $2 \times 2 \times 2$ unit cell barium zirconate system is shown. The oxygen sites nearest, second nearest, and third nearest neighbors to the yttrium are shown in decreasing shading of red, respectively. Zirconium ions are shown in green; yttrium is shown in teal. Barium ions have been removed for clarity.

1.5 Proton binding sites

Similar to the distinct categories in oxygen ion sites, proton binding sites were divided into eight distinct categories which are highlighted by a different color in Fig. 1.4. Protons in the same categories have the same distance away from a dopant, distance distributions, and hydrogen bonding pattern with nearby oxygen ions. As shown in Fig. 1.3, oxygen ions are nearest (I), second nearest (II), or third nearest (III) from the dopant. Further, as seen in Fig.1.2 (c), every face has

a closer pair of oxygen ions and a further pair. The H_I^{Close} protons in Fig. 1.4 are on dopant nearest neighbor oxygen ions and hence labeled as I in subscript. The close superscript label notes that the oxygen ion that the proton is on is part of a closer oxygen ion pair. The H_I^{Far} protons are also on a dopant nearest neighbor oxygen ion. However, the oxygen ion binding the proton is part of a farther apart oxygen ion pair. Using the same strategy protons on the dopant third nearest neighbor oxygen ion are called H_{III}^{Close} and H_{III}^{Far}. The H_{IID}^{Close} and H_{IID}^{Far} protons are protons on dopant third nearest neighbor oxygen ions with hydroxyls pointing into faces that contain the dopant. Respectively, the H_{IIND}^{Close} and H_{IIND}^{Far} protons are on dopant second nearest neighbor oxygen ions with hydroxyls pointing into faces that do not contain the dopant.

Protons can also move between sites by rotation, intra-octahedral(R) transfer or inter-octahedral(I). Rotation moves between proton sites on the same oxygen ion, for instance H_I^{Close} to H_I^{Far} as indicated by a blue/orange curved line labeled R. Intra-octahedral transfer refers to the movement of a proton from a site on an ion to a site on an oxygen ion on the same octahedron, for instance H_I^{Close} to H_I^{Far} as indicated by the blue/brown solid straight line labeled as T. Inter-octahedral transfer refers to a movement from a proton site on an oxygen ion in one octahedron to site on an oxygen ion on a different octahedron, for instance H_I^{Close} to H_{IID}^{Close} as indicated by the blue/teal straight line labeled I.

1.6 Expansion of unit cell

Our early studies showed that both protons and oxygen vacancies in a $2\times2\times2$ unit cell system can disrupt tilting patterns through the entire small periodic system. To avoid periodic small system size issues, a simulation box of $4 \times 4 \times 4$ unit cell system was used when introducing vacancies and protons, rather than the $2 \times 2 \times 2$ unit cell system used to find the best Glazer tilting arrangement. The large system is created by replicating the optimum Glazer tilting arrangement twice in each direction. A single gamma point was used to generate the plane wave basis set for the $4 \times 4 \times 4$ unit cell systems. Cell size was fixed at the optimum size found in the small system. Otherwise, the same electronic structure method and ionic conjugate gradient optimization is used as that described above for the Glazer distortions. Testing on selected structures showed that for the larger system, relative energies found with a single gamma point where similar to those found using the $2 \times 2 \times 2$ k-point mesh.

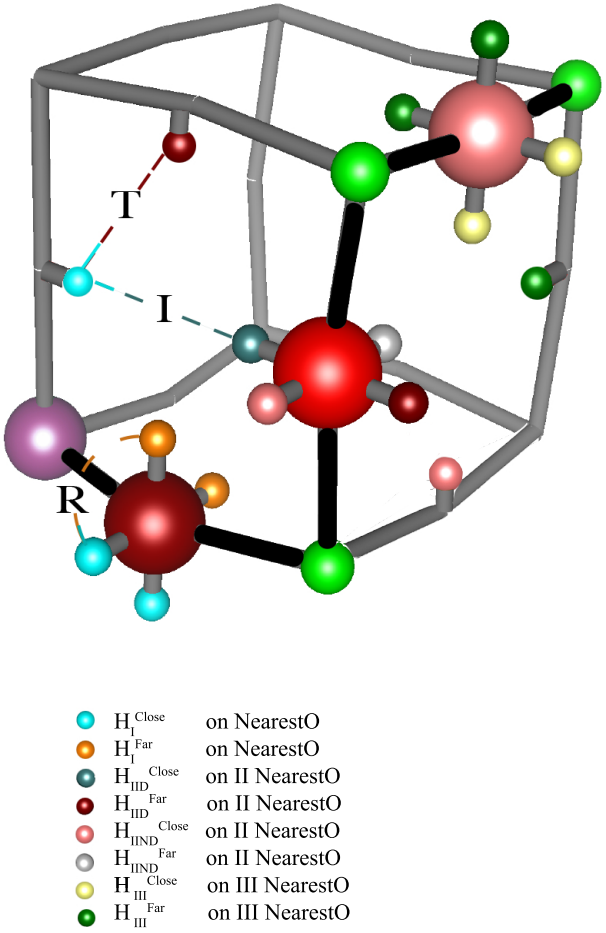

FIGURE 1.4: There are eight distinct categories of protons, highlighted by different colors in the legend. Protons in the same categories have the same distance away from a dopant, distance distributions, and hydrogen bonding pattern with nearby oxygen ions. The proton site categories are labelled through subscript and superscript, for instance, the H_I^{Close} protons are dopant nearest neighbor oxygen ions and hence labeled as I in subscript. The close superscript label notes that the oxygen ion that the proton is on is part of a closer oxygen ion pair. Protons can also move between sites by rotation, intra-octahedral(R) transfer or inter-octahedral(I). Rotation moves between proton sites on the same oxygen ion, for instance H_I^{Close} to H_I^{Far} as indicated by a blue/orange curved line labeled R. Intra-octahedral transfer refers to the movement of a proton from a site on an ion to a site on an oxygen ion on the same octahedron, for instance H_I^{Close} to H_I^{Far} as indicated by the blue/brown solid straight line labeled as T. Inter-octahedral transfer refers to a movement from a proton site on an oxygen ion in one octahedron to site on an oxygen ion on a different octahedron, for instance H_I^{Close} to H_{IID}^{Close} as indicated by the blue/teal straight line labeled I.

Chapter 2

Computational methods

2.1 Potential energy surface and born oppenheimer approximation

Potential Energy Surfaces (PES) describe the energy of a molecule as a function of its geometry. One way to calculate the energy is to use wave function or density functional theories to solve the Schrodinger equation $\widehat{H}\Psi = E\Psi$. The Hamiltonian ($\widehat{H}$) in the Schrodinger equation can be expressed as a sum of kinetic ($\widehat{T}$) and potential (V) energy operators. R is the nuclear coordinate. r is the electronic coordinate. Most parts of the Hamiltonian which is shown in Eq. 2.1 can be separated into nuclear or electronic components except $V_{eN}(r, R)$.

$$\widehat{H} = \widehat{T}_N(R) + \widehat{T}_e(r) + V_{eN}(r, R) + V_{NN}(R) + V_{ee}(r) \tag{2.1}$$

The Born-Oppenheimer approximation states that since the mass of the nuclei greatly exceeds that of the electron, the nuclei can be viewed as fixed points. This allows a separation of the Schrodinger equation into two equations - one for the nuclei which are treated classically and another for the electrons which are treated quantum mechanically. The Hamiltonian for the electrons becomes:

$$\widehat{H}_{electronic} = \widehat{T}_e(r) + \widehat{V}_{eN}(r, R) + \widehat{V}_{NN}(R) + \widehat{V}_{ee}(r) \tag{2.2}$$

Wave function quantum mechanics tries to find the wave function that minimizes the expectation value of the Hamiltonian minimizing the energy. According to the variational principle, the wave function energy calculated is always greater than or equal to the actual energy:

$$E_\varphi \geqslant E_0 \tag{2.3}$$

The trial wave function Φ_{trial} is the sum of basis set functions (psi_i) weighted by coefficients (c_i):

$$\Phi_{trial} = \sum c_i \psi_i \tag{2.4}$$

and is inserted into the Schrodinger equation to solve for the energy:

$$E_{trial} = \frac{\langle \Phi_{trial} | \widehat{H} | \Phi_{trial} \rangle}{\langle \Phi_{trial} | \Phi_{trial} \rangle} \tag{2.5}$$

The variational principle claims that when the coefficients (c_i) of the basis set functions are changed until the energy minimized the resulting energy is still an upper bound to the true ground state energy. Hartree-Fock is a variational method.

However, density functional theory (DFT) is not strictly variational in its convergence properties despite the similarity between the Kohn-Sham equations solved and the Hartree-Fock equations. However, wave functions are still used in method and including more is generally better.

2.2 Density functional theory and vienna ab initio simulation package

Density functional theory (DFT) in the Vienna Ab initio Simulation Package (Vasp)[5, 15–18] are used to generate the PES on which atoms move. DFT uses a trial electron density. This idea was proposed by Walter Kohn and Pierre Hohenberg, who laid the foundation of DFT via two theorems. The first Hohenberg and Kohn theorem suggest that density can be used to replace the potential as the basic function to categorize the system [19, 20]. The functional for energy can be written in terms of a density field and the energy can be minimized variationally using the Levy Constrained-Search formalism[21].

$$E_0 \leq E[\rho] + T[\rho] + E_{Ne}[\rho] + E_{ee}[\rho] \tag{2.6}$$

The second Hohenberg and Kohn theorem suggest that there exist a universal functional F[n], such that for any density n(r), the energy functional is:

$$E_0 = \min(F[n] + \int d^3r \; v_{ext}(r)n(r)) \tag{2.7}$$

The universal functional F[n] is given by the following equation, with T being the kinetic energy component, V_{ee} being the electron-electron repulsion component.

$$F[n] = min\langle\psi|\widehat{T} + \widehat{T}_{ee}|\Psi\rangle \tag{2.8}$$

DFT is a very useful tool mainly due to its simplicity, as the electron density depends only on 3 variables x, y, z, where as the wave function depends on 4 variables (x, y, z, spin) for every electron in the system giving 4N variable dependence. Admittedly, there is a deficiency in this method in that the true universal functional is unknown. However, various approximations have been made, for instance Local Density Approximation (LDA) and Generalized Gradient Approximation (GGA). The latter is done in a variety of flavors including the approach by Perdew-Burke-Ernzerhof yielding the PBE functional which is used in this study.

Vasp[5, 15–18] performs ab-initio density functional theory energy and force calculation using a plane wave basis set for valence electrons and pseudopotentials or the projector-augmented wave (PAW) descriptions of inner core electrons. For the calculation in this paper, the Perdew-Burke-Ernzerhof (PBE) functional and projection augmented wave function (PAW) are used to simplify inner core electron treatment. Periodic boundary conditions are also used to avoid edge effects and

mimic an extended solid. A periodic plane wave basis set is also used to capture the periodic nature of the electron density in a periodic solid structure. The plane waves are generated on a grid of frequencies controlled by K-point, one of the essential parameters in VASP to control accuracy. K-point controls the spacing between plane wave functions. As K-point increase, the spacing between waves decrease, and the more accurate the potential energy calculation will be. Another way to increase the accuracy is to increase the energy cutoff. However, unlike K-point, increasing energy cutoff does not alter the spacing between the wave basis functions, but raises the bar of energy cut-off, so that more plane waves fall below the cut-off. Increasing the K-point mesh and the energy cutoff can both increase the accuracy of the calculation but at increased computational expense. In conclusion, in this study, VASP is used to find the electronic energies of the system through DFT, and to move on this Born-Oppenheimer surface. The conjugate gradient algorithm is used to find minima on the Born-Oppenheimer surface or potential energy for the nuclei. The NEB method which is incorporated in VASP can minimize energy pathways.

2.3 Nudged elastic band method

PES not only describes the energy but also offer information through stationary points including: minima, transition states, and saddle points. In this study, the minima are found using the conjugate gradient method. Lowest energy paths between the minima are found using the Nudged Elastic Band (NEB) method. The climbing Nudged Elastic Band (cNEB) method is then used to find the transition

state on the minimum energy path. The NEB minimum energy path calculation is an efficient method to find the minimum energy path (MEP), a path that connects the initial and final states. The transition path is found by placing a set of images between the initial and final states. In Fig. 2.1, 4 images are evenly spaced between the initial state and final state. Initially, a band (dashed) is placed by directly connecting the initial state and final states, represented by red circles. 4 interpolated images, represented by black circles, are positioned equidistantly along the dashed band. The coordinates for the intermediate images are generated by dividing the configuration difference $\overrightarrow{d}$ between the initial state and final state, by the corresponding desired number of images (n) plus one. For instance, the first out of n intermediate images will have the initial configuration vector plus $\overrightarrow{d}$/(n+1), and the second images will have initial configuration vector plus $2\overrightarrow{d}$/(n+1) and so on. After minimization, the band and the intermediate images relocate and is represented by the solid line.

A spring force is added between images allowing path movement mimicking the motion of an"elastic band". The "nudging" part mainly comes from the perpendicular component of the true force. There are two forces involved in NEB, the perpendicular component of the true force and the parallel component of the spring force. The perpendicular component of the true force bring the intermediate transition images closer to the MEP, while the parallel component of the true force drag them towards the minima, interfering with the convergence of the elastic band to the MEP, therefore, only the perpendicular component of the true force is kept. However, the perpendicular component of the force brings it closer

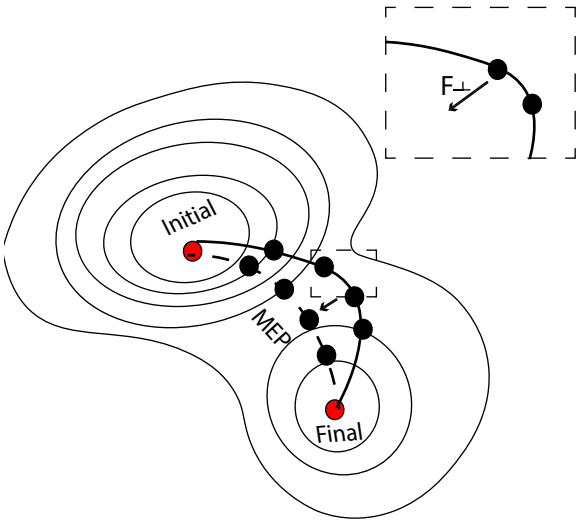

FIGURE 2.1: The 3D Nudged Elastic Band (NEB) minimum energy path with 4 intermediate images between the initial state and final state. The perpendicular component of the force bring the path closer to MEP.

to MEP, as shown in the upper right corner of Fig. 2.1.

Climbing NEB is an addition of the NEB method that brings a better convergence to the saddle point without increasing the computational expense. Once the MEP is found through NEB, image with the highest energy is driven towards the saddle point, by inverting the forces along the path for that image.

In this study, the energy optimized was the DFT energy with the PBE functional in VASP[5, 15–18]. A plane wave basis set generated from a $2 \times 2 \times 2$ k-point mesh was used with energy cutoff of 600 eV. A background charge compensating cloud was used. The twenty three possible Glazer distortions[6] for a $2 \times 2 \times 2$ unit cell system of barium zirconate with one dopant defect (D'_{Zr}) or a 12.5% doping level were generated. Each configuration was optimized using the conjugate gradient method allowing both ions and cell size to vary. The convergence stopping criterion required forces to be less than 0.01 eV/Å. Also a simulation box of $4 \times 4 \times 4$ unit

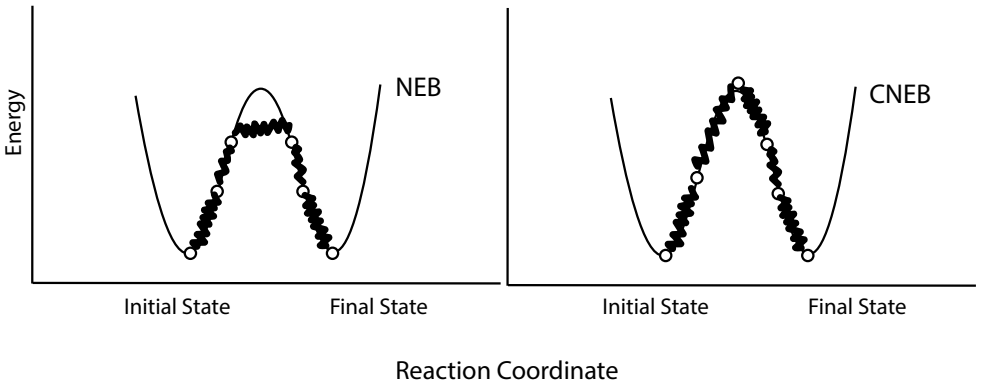

FIGURE 2.2: The 2D Nudged elastic band (NEB) and Climbing Nudged elastic band (CNEB) with 4 intermediate images between the initial state and final state. The CNEB brings one images right to the saddle point and gives the activation energy precisely with no additional computational expense.

cell system was used when introducing vacancies and protons, rather than the $2 \times 2 \times 2$ unit cell system used to find the best Glazer tilting arrangement. The large system is created by replicating the optimum Glazer tilting arrangement twice in each direction. A single gamma point was used to generate the plane wave basis set for the $4 \times 4 \times 4$ unit cell systems. Cell size was fixed at the optimum size found in the small system. Otherwise, the same electronic structure method and ionic conjugate gradient optimization is used as that described above for the Glazer distortions. Testing on selected structures showed that for the larger system, relative energies found with a single gamma point where similar to those found using the $2 \times 2 \times 2$ k-point mesh. The NEB followed by cNEB method [22–24] with two images, spring constants of 5.0 eV/Å^2, and force optimizers was used to find activation barriers for oxygen vacancy motion with force convergence criteria set to 0.02 eV/Å.

2.4 Kinetic monte Carlo

Kinetic Monte Carlo is able to solve one of the time-scale limitations of Molecular Dynamics, so that it can simulate systems involving annihilation of defects that occur over a much longer time period. Kinetic Monte Carlo refers to the algorithms to simulate the propagation of system through the introduction of random number [25]

Consider an ordered list of all possible transitions from the current state with associated rates, the probability to go from the current state X_i to any state X_j is as $\frac{k_{ijl}}{\sum^l k_{ijl}}$, and the partial sum of rate k_{ij} for all transitions from the current state to any state X_j can be expressed as:

$$S_{jl} = k_{ijl} = k_{ij1} + k_{ij2} + k_{ij3} + ... + k_{ijl} \tag{2.9}$$

An illustration of the ordered list are shown below, with S_j represented by the length of all the objects up to and including j:

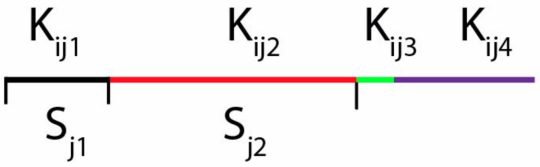

FIGURE 2.3: Illustration of partial sum using ordered line, with S_j represented by the length, the longer the line segment, the higher the probability.

A random number n is then chosen, with n $\in$ (0, $\sum^l k_{ijl}$] , and the landing point of the random number is used to determine the next step by selecting an event m

for which $S_{jm-1} < \mathrm{n} < Sj_m$. In other words, if $\mathrm{n} < S_{jm}$ then the transition from X_i to X_m would be carried out. However, if $\mathrm{n} > S_{jm}$, additional sum k_{ijm} will be added until partial sum S_{jm} is greater than n, and then the state X_i would be updated to X'_m.

After the state is updated, the time also needs to be advanced.The new time is the addition of the current time with typical time to do the chosen move. The time to do the chosen move is selected from distribution, in this case the poisson distribution. The code to generate the initial file are in Appendix A.1.

Chapter 3

Optimum tilting structure of Sc doped $BaZrO_3$

3.1 Lowest energy structure in 23 Glazer possible glazer distortion and lattice constant

There are 23 Glazer distortion in a 2x2x2 Sc doped perovskite composed of 14 3-tilt systems, 6 2-tilt systems, 2 1-tilt systems, and 1 0-tilt systems. Distortions are labelled according to the Glazer's notation, where + refers to subsequent layers tilting in the same directions, - in opposite directions, and 0 to no tilt [6]. The relative energies for the initial 23 Glazer structures, optimized using VASP are shown in Appendix A.1. After expanding the initial 2x2x2 system in each direction to obtain a 4x4x4 system, the lowest energy structure is found. The lowest energy

structure is number 4 with structure (-,-,-), energy -325.34 eV. The second lowest energy structure is number 17, with structure (+,+,-), energy -325.31eV.

The lowest energy Glazer distortion pattern[6] found for Sc system was (-,-,-) or showed opposite octahedral tilting pattern in alternate layers perpendicular to the x, y, and z directions. This is the same Glazer tilting pattern found in our earlier studies of the yttrium doped system[2]. This study, however, uses a force convergene 0.01 eV/Å rather than the default one used for earlier work.

Table 3.1 shows the Shannon ionic radii, Shannon calculated lattice size, and optimized lattice constant of Sc and two other differently sized dopants. For scandium ion, the ionic radii is 0.745 Å , the calculated lattice size for scandium doped barium zirconate is 4.25 Å , and the optimized lattice constand is 4.26 Å . In comparison, the smaller aluminum ion has a smaller ion radius, calculated lattice size and optimized lattice size, 0.535 Å and 4.20 Å , 4.24 Å ; while the larger yittrium ion has a larger ion radius, lattice size, and optimized lattice size, 0.90 Å , 4.29 Å and 4.29 Å . This is in well agreement with Fig. 3.1, which shows a section of simulation box for each system.

Additionally, even though the experimental lattice constants is not exactly the same as the optimized lattice constant, the difference between the dopants are in perfectly good agreement, for instance, the difference between Sc and Y is 0.03 in both the optimized lattice constant and the experimental one.

TABLE 3.1: The Shannon ionic radii, lattice size assuming close packing with Shannon ionic radii, lowest energy lattice size found using DFT in this study, and experimental lattice constants are shown for systems with each of the dopant defects considered. Optimized lattice constants for the undoped system can vary greatly from 4.10 to 4.40 Å with exchange correlation functional and pseudopotential choice[7]. The variation found with dopant in this system is smaller than the variation found with functional choice.

Defect	Ion Radius (Å)	Shannon Calculated Lattice Constants (Å)	Average Optimized Lattice (Å) Constants	Experimental Lattice Constants (Å)
Al'_{Zr}	0.535	4.20	4.24	
Zr_{Zr}	0.72	4.25	4.25	4.19 [26]
Sc'_{Zr}	0.745	4.25	4.26	4.20 [8]
Y'_{Zr}	0.90	4.29	4.29	a=4.23, c=4.21 [27]

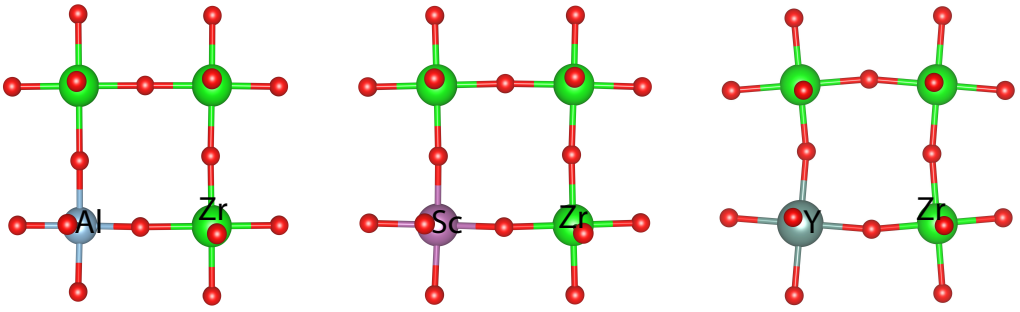

(a) (b) (c)

FIGURE 3.1: The structure of a small section of the Al (a), Sc (b), and Y(c) systems, respectively, is shown to visually highlight increased tilting with increasing dopant ion size. As tilting increases, a pair of oxygen ions gets closer together while the other pair gets further apart.

3.2 Octahdral tilting pattern

Fig. 3.1 also shows that as dopant size increase, one pair of oxygen ions in each face come closer together while another gets further apart, thereby, increasing octahedral tilting.

Similar result has been observed in Fig. 3.2. The ZrOX angle distributions are shown for the (b) Al, (c) Sc , (d) Y doped systems as solid grey rectangles when X=Zr and lighter grey rectangles when X=D where D is the dopant. As shown in (b), (c), (d), as dopant size increase, the ZrOD angle (lighter grey rectangles) shifts further away from the 180 degree on the right. Notice that the solid grey rectangle reside within the 170-175 angle region for all three dopant system, however the position of lighter grey rectangle change from systen to sytem. The lighter grey rectangle Zr-O-Sc angle distribution remains within the grey solid rectangle Zr-O-Zr angle distribution. In comparison, Zr-O-Al angle distribution shifts closer to 180 (less tilting) than the corresponding grey solid rectangle Zr-O-Zr angle distribution; while the lighter grey rectangle Zr-O-Y angle distribution shifts away from 180 relative to the grey solid rectangle Zr-O-Zr angle distribution. Therefore, octaheral tilting increase as dopant size increase.

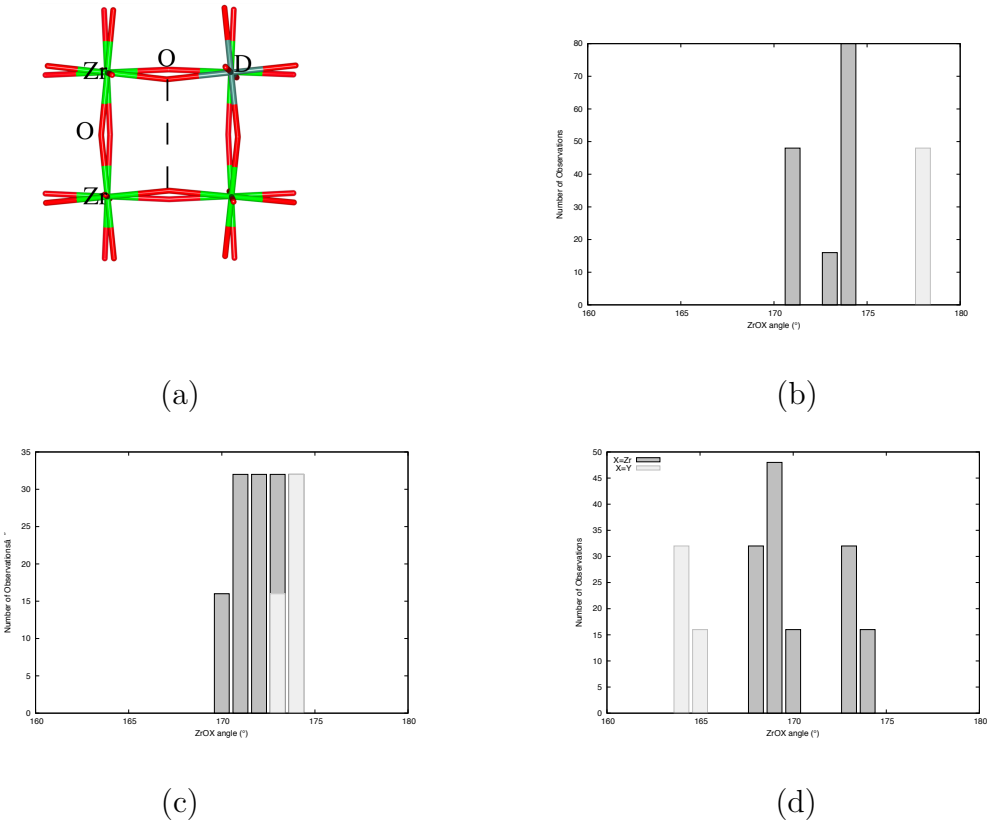

FIGURE 3.2: (a) shows the ZrOD angle in a section of Y system in stick model. The ZrOD angle always refers to the smaller angle in the plane. The ZrOX angle distributions are shown for the (b) Al, (c) Sc, (d) Y doped systems as solid grey rectangles when X=Zr and lighter grey rectangles when X=D where D is the dopant. As the dopant size increases, there is a greater shift away from the 180 for Zr-O-D angles relative to Zr-O-Zr angles.

3.3 The impact of oxygen vacancies on octahedral tilting

The presence of oxygen vacancy at three distinct location(dopant nearest, second nearest, and third nearest neighbor oxygen site) further alters local octahedral tilting by introducing a broadening of ZrOX distributions shown in Fig. 3.3. While

the broadening is similar for all types of vacancies, the Boltzmann probabilities at 800K between systems with different types of vacancies are significantly different shown in Table 3.2. For scandium systems, nearest neighbor oxygen sites are the most likely position for an oxygen vacancy, suggesting that a study of proton conduction in scandium doped barium zirconate only need to consider the possibility of nearest oxygen vacancy. In aluminum system, similarly, the most likely position is nearest site. However, in the yttrium system, finding the vacancy at a nearest neighbor oxygen site is only about twice as likely as finding it at a second nearest neighbor oxygen site. This suggests that study of proton conduction in Y system needs to consider both vacancy location possibilities. Additionally, in all dopant systems, the lowest energy oxygen vacancy occurs at an dopant nearest neighbor oxygen site which is expected as positive and negative defects attract. The remaining energy pattern shown in Table 3.2 is a complex interplay of octahedral tilting induced by the dopant and by the oxygen vacancy.

TABLE 3.2: Optimizing a 12.5% doped system with a dopant nearest, second nearest, and third nearest neighbor oxygen vacancy gives the relative energies and 800K Boltzmann exponential probability factors shown at the minima.

	Al		Sc		Y	
	Energy (eV)	Probability at 800K	Energy (eV)	Probability at 800K	Energy (eV)	Probability at 800K
Nearest	0.00	1.00	0.00	0.98	0.00	0.67
2nd Nearest	0.98	0.00	0.43	0.00	0.05	0.33
3rd Nearest	0.53	0.00	0.29	0.02	0.41	0.00

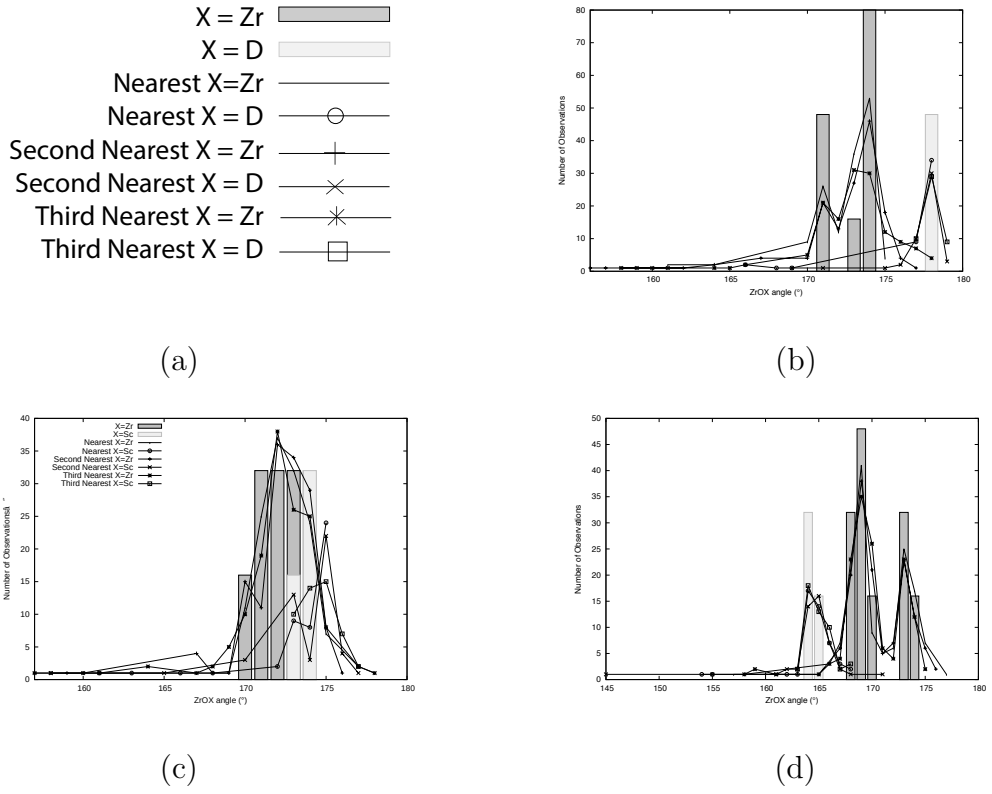

FIGURE 3.3: (a) shows the legend for angle distributions. The ZrOX angle distributions are shown for the (b) Al, (c) Sc, (d) Y doped systems as solid grey rectangles when X=Zr and lighter grey rectangles when X=D where D is the dopant. When there is a dopant nearest neighbor oxygen vacancy, a solid line and a line with open circles mark the ZrOZr and ZrOD distributions. When there is an dopant second nearest neighbor oxygen vacancy, ZrOZr and ZrOD angle distributions are shown with a dashed line and crossed line, respectively. Finally, ZrOZr and ZrOD angle distributions when there is a dopant third nearest neighbors oxygen vacancy are highlighted with starred and squared lines. When the vacancy is introduced, the distributions broaden.

Chapter 4

Oxygen vacancy

4.1 The effect of oxygen vacancy conduction on Sc doped $BaZrO_3$

Since in scandium doped barium zirconate, the major focus is on nearest oxygen vacancy, a kinetic Monte Carlo study including oxygen vacancy motion only need to include vacancy motion between sites closest to the dopant in the scandium systems, as shown in Fig. 4.1 (a), where oxygen vacancy moves from an dopant nearest neighbor oxygen site to another nearest neighbor site in Sc system through a 0.01 eV barrier. In Fig.4.1, moving oxygen ions are highlighted in black, and the vacancy location are highlighted in a square box in the first and last image. The two images in the middle shows the transition vacancy motion from the initial image to the final one. Other transitions are also shown in Fig. 4.1.

Fig. 4.1 (b) shows oxygen vacancy moving from an dopant nearest neighbor oxygen

site to a dopant second nearest neighbor oxygen site through a larger 0.72 eV barrier. In Fig. 4.1 (c), the vacancy moves from a dopant second nearest neighbor oxygen site to a third nearest neighbor site through a 0.48 eV barrier. Similar transitions also occur for Al and Y case.

TABLE 4.1: The forward (E_f) and backward (E_b) energies barriers are given for each type of oxygen vacancy transition in eV. I, II, and III refer to having the vacancy at a first, second, or third nearest neighbor oxygen site from the Sc dopant.

$V_O^{\bullet\bullet}$ Transition	E_f (eV)	E_b (eV)
I to I	0.01	0.01
I to II	0.72	0.29
II to III	0.48	0.62

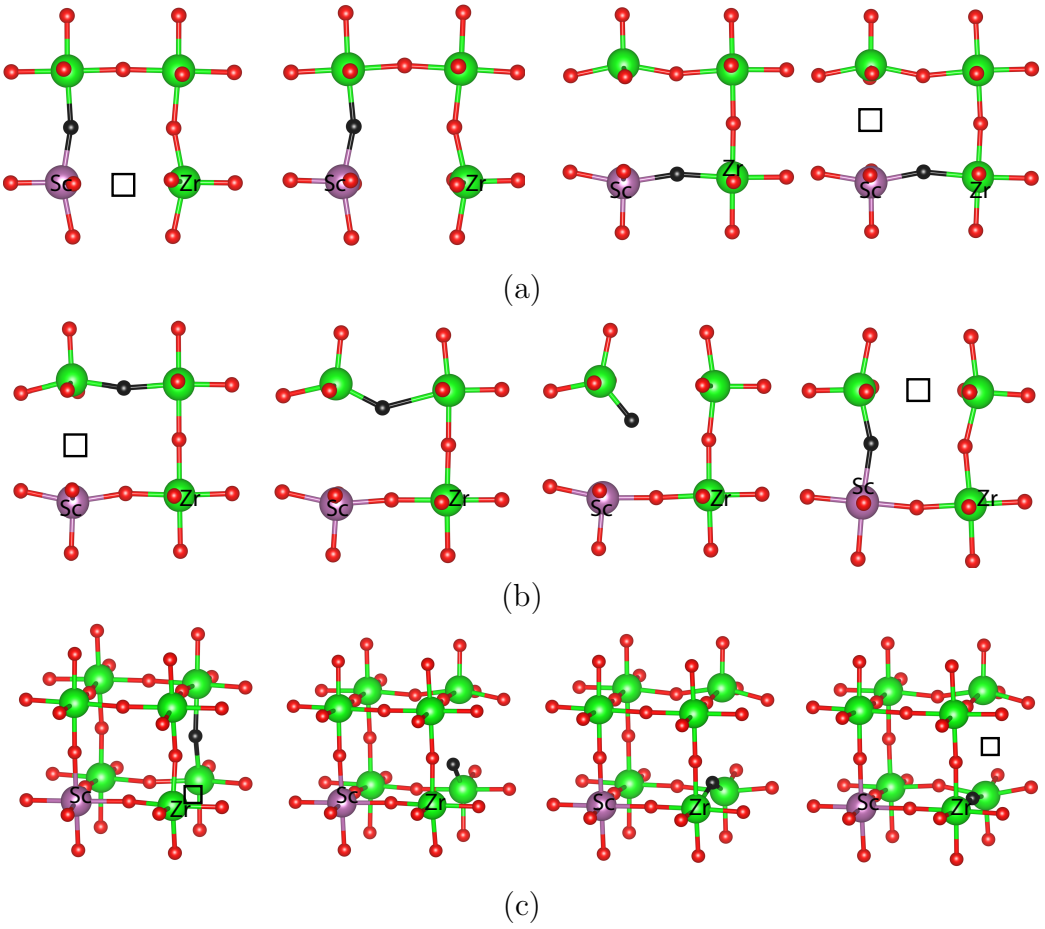

FIGURE 4.1: NEB and cNEB with two images show the transition state of oxygen vacancy conduction. Sc system with moving oxygen ions highlighted in black, and the vacancy location highlighted in a square box in the first and last image of (a), (b) and (c). (a) $V_O^{\bullet\bullet}$ moves from an oxygen site adjacent to the dopant to another adjacent site in Sc system through a 0.01 eV barrier. (b) $V_O^{\bullet\bullet}$ moves from an oxygen site adjacent to the dopant to an oxygen site once removed from the dopant through a larger 0.72 eV barrier. (c) $V_O^{\bullet\bullet}$ moves from an oxygen site once removed from the dopant to one twice removed from the dopant through a 0.48 eV barrier.

Chapter 5

Proton conduction

5.1 The effect of oxygen vacancy on proton conduction

Since the oxygen vacancy at nearest oxygen site has the lowest energy as shown in Table 5.1, its effect on proton binding sites and proton conduction was carefully studied. However, before introducing oxygen vacancy at the nearest oxygen site, the case without oxygen vacancy is explored.

In the absence of oxygen vacancy, different protons on the same type of proton category have roughly the same energy with slight variation (about 0.02 eV) depending on hydroxyl tilting, as shown in Fig. 5.1. Fig. 5.2 shows the relative energies of each proton site category for each proton group as a function of distance. The order of the relative energies of different proton sites order is mirrored

in the legend, with H_{2D}^{Close} having the highest energy, and H_{I}^{Far} having the lowest energy.

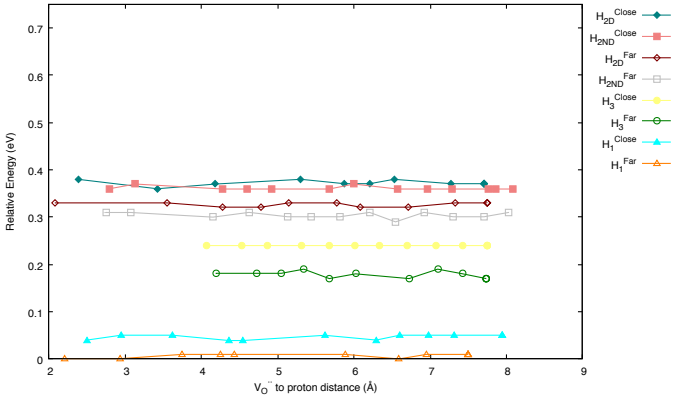

FIGURE 5.1: Relative energy is shown as a function of proton distance. The legend order mirrors the relative energies order in the case with oxygen vacancy.

When oxygen vacancy is presence, protons in each category in Fig. 1.4 have distinct distances to the oxygen vacancy and hence have different energy. Fig. 5.2 shows the relative energies of each proton site category for each proton group as a function of distance away from an oxygen vacancy adjacent to the dopant, the order of the relative energies is also mirrored in the legend. All proton binding sites near the vacancy up to 6 Å are included. Beyond this distance, only about one in 3 protons are included since at this point the energies fluctuate less. While the long range energies for each type of proton plateau, there are significant fluctuations at distances closer to the vacancy.

By comparing Fig.5.1 and Fig.5.2, it is found that the relative energies of the different proton sites at large distances away from vacancy are the same as those in the absence of vacancy. If all the proton category relative energies in the absence of oxygen vacancy are shifted up by 0.15 eV for the scandium dopant systems, these

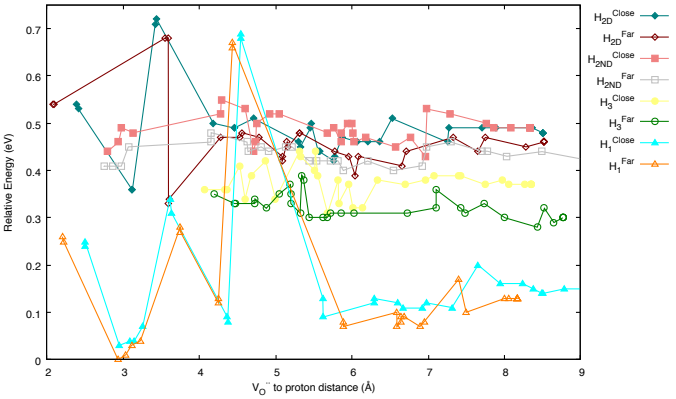

FIGURE 5.2: Relative energy is shown as a function of proton distance from the oxygen vacancy for Sc doped system. The legend order mirrors the relative energies at large distance away from vacancy.

energies roughly align with energies in the presence of the vacancy when proton is at large distance away from the vacancy.

However, at small distance away from the vacancy, there are large fluctuations in energy of the proton binding sites, which enable proton conduction to take place. As can be seen in Fig. 1.3, for long range proton conduction to appear, proton motion in planes containing the dopant requires movement between type I and II oxygen ions; while in planes without the dopant, moves through type II and III oxygen ions are needed. Furthermore, in order for proton to get away from the type I oxygen site to type II site, the energy between type I and type II must be close enough. In scandium system, many proton sites on type II oxygen ions are quite close to energy of proton sites on type I oxygen ions, suggesting possible conduction. As for the other systems, the Al system is a poor proton conductor, since there is a huge energy gap between proton sites on oxygen ions nearest to the dopant and protons on second nearest oxygen ions sites; while Y system has the smallest gap, making conduction very favorable.

5.2 Proton trajectory to escape from trapping site

Tables 5.1 show the relative initial, transition state, and final energies for all the possible rotations (R), intra-octahedral transfer (T), and inter-octahedral transfer (I) without oxygen vacancy for all three systems. Earlier studies[10, 11] showed that proton conduction in the smallest Al system occurred through periodic escapes from the dopant trap to planes without the dopant where the proton could travel quickly through a fast conduction pathway before getting trapped again at another dopant site, while proton conduction in the largest Y system kept the proton near the trap. In this study, proton conduction in the middle Sc system is studied and compared with the other two systems. It is found that like Y system, proton conduction in the Sc system moved through proton sites on type I and II oxygen ions; while proton conduction move through all three types (I, II, and III) oxygen site in Al system.

Table 5.1 highlights the potential pathway to get away from the lowest energy binding site in bold. In the Sc system, the lowest energy site is H_I^{Far}, with relative energy 0.00eV. Both a rotation and intra-octahedral can move the proton from the lowest energy sites H_I^{Far} to H_I^{Close} through a 0.05 eV barrier. The proton can continue to move through very low barriers between type I proton sites. However, to escape to a type II site, the proton need to cross a lowest barrier of 0.47 eV in the T(H_I^{Close}, H_{IID}^{Far}) intra-octahedral transfer. From H_{IID}^{Far}, the lowest barrier to escape is a barrierless rotation transfer to H_{IIND}^{Far}. From there, the lowest barrier

is a return to H_{IID}^{Far} (trap site) with 0.02 eV barrier. This proton trajectory shows that for Sc system, getting away from the trapped type I sites take the most energy, but movements between type II take very little energy, and is visualized in Fig.5.3. The sample path in Sc system display a similar trend as Y system that proton does not proceed to type III oxygen sites since they are trapped at type II due to trapping.

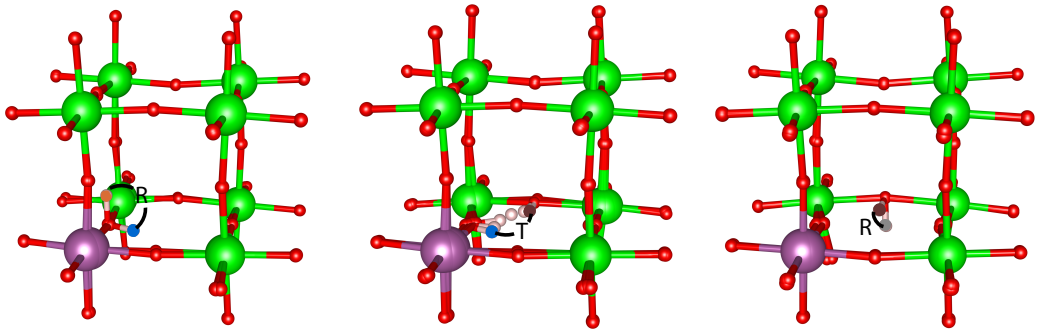

FIGURE 5.3: The proton trajectory to escape from type I site to type II site in Sc system. Proton travels from the lowest energy type I site H_I^{Far} (orange) to another type I site H_I^{Close}(blue), via either rotation or intra-octahedral transfer. To escape to a type II site, proton travels through intra-octahedral transfer to H_{IID}^{Far})(brown) by crossing a lowest barrier of 0.47 eV. Proton can then moves to another type II site via rotation, but can not proceed forward to type III site

TABLE 5.1: The relative energies of the initial site (i), transition state (TS), and final site (f) are shown for rotation (R) and intra-octahedral transfer (T) in eV for doped systems without oxygen vacancies.

Move(i,f)	**Sc** i	TS	F	**Y** i	TS	F
R(H_I^{Far}, H_I^{Far})	0.00	0.16	0.01	0.05	0.06	0.06
R(H_I^{Far}, H_I^{Close})	**0.00**	**0.05**	**0.05**	0.05	0.14	0.14
T(H_I^{Far}, H_{IID}^{Close})	0.01	0.53	0.36	0.05	0.18	0.16
T(H_I^{Far}, H_I^{Close})	0.00	0.05	0.05	0.04	0.28	0.10
R(H_I^{Close}, H_I^{Close})	0.05	0.06	0.05	0.14	0.14	0.10
R(H_I^{Close}, H_I^{Far})	0.05	0.05	0.00	0.14	0.14	0.05
T(H_I^{Close}, H_{IID}^{Far})	**0.05**	**0.52**	**0.33**	0.11	0.11	0.03
T(H_I^{Close}, H_I^{Far})	0.05	0.05	0.00	0.10	0.28	0.04
R(H_{III}^{Far}, H_{III}^{Far})	0.17	0.31	0.19	0.25	0.27	0.26
T(H_{III}^{Far},H_{IIND}^{Close})	0.17	0.37	0.37	0.26	0.28	0.23
R(H_{III}^{Far}, H_{III}^{Close})	0.18	0.25	0.24	0.25	0.30	0.30
T(H_{III}^{Far}, H_{III}^{Close})	0.18	0.47	0.24	0.25	0.33	0.30
R(H_{III}^{Close}, H_{III}^{Close})	0.24	0.25	0.24	0.30	0.33	0.31
R(H_{III}^{Close}, H_{III}^{Far})	0.24	0.25	0.18	0.30	0.30	0.25
T(H_{III}^{Close}, H_{III}^{Far})	0.24	0.47	0.18	0.30	0.33	0.25
T(H_{III}^{Close},H_{IIND}^{Far})	0.24	0.36	0.31	0.32	0.32	0.18
R(H_{IIND}^{Far},H_{IID}^{Close})	0.31	0.38	0.38	0.18	0.18	0.14
R(H_{IIND}^{Far},H_{IID}^{Far})	0.31	0.33	0.33	0.20	0.24	0.0
T(H_{IIND}^{Far}),H_{IIND}^{Close})	0.31	0.60	0.36	0.18	0.23	0.23
T(H_{IIND}^{Far},H_{III}^{Close})	0.31	0.36	0.24	0.18	0.32	0.32
R(H_{IIND}^{Close},H_{IID}^{Far})	0.36	0.36	0.33	0.23	0.25	0.01
R(H_{IIND}^{Close},H_{IID}^{Close})	0.36	0.38	0.37	0.23	0.23	0.16
T(H_{IIND}^{Close}),H_{IIND}^{Far})	0.36	0.36	0.18	0.23	0.23	0.18
T(H_{IIND}^{Close},H_{III}^{Far})	0.36	0.37	0.18	0.23	0.28	0.26
T(H_{IID}^{Far},H_I^{Close})	0.33	0.52	0.05	**0.03**	**0.11**	**0.11**
T(H_{IID}^{Far}, H_{IID}^{Close})	0.32	0.39	0.37	**0.00**	**0.15**	**0.14**
R(H_{IID}^{Far},H_{IIND}^{Far})	**0.33**	**0.33**	**0.31**	0.00	0.24	0.20
R(H_{IID}^{Far},H_{IIND}^{Close})	0.33	0.36	0.36	0.01	0.25	0.23
R(H_{IID}^{Close},H_{IIND}^{Close})	0.37	0.38	0.36	0.16	0.23	0.23
T(H_{IID}^{Close},H_{IID}^{Far})	0.37	0.39	0.32	0.14	0.15	0.00
T(H_{IID}^{Close},H_I^{Far})	0.36	0.53	0.01	0.16	0.18	0.05
R(H_{IID}^{Close},H_{IIND}^{Far})	0.38	0.38	0.31	0.14	0.18	0.18

Notice that Table 5.1 does not show the relative energies of the initial site (i), transition state (TS), and final site (f) for inter-octahedral transfer for Sc system. This is because, in Sc system, there is no direct inter–octahedral transfer. In

fact, inter–octahedral transfer occurs through a double intra-octahedral transfer,as displayed in Fig.5.4, the energy of the transition is not listed.

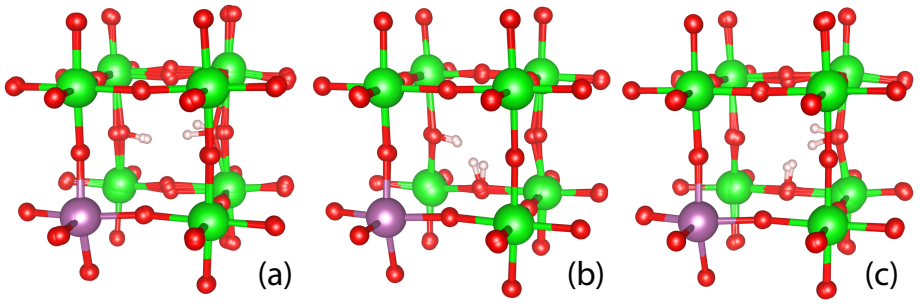

FIGURE 5.4: Inter transition (a) in Sc system is made possible via two intra transition(b)(c). (a) shows a sample inter–octahedral transfer. (b) and (c) is the actual indirect intra–octahedral proton transfer.

Table 5.2 shows the relative initial, transition state, and final energies for all the possible rotations (R), intra-octahedral transfer (T), and inter-octahedral transfer (I) in the presence of oxygen vacancy. The transitions starts from proton of each type that is closest to the vacancy.

In Sc system, the barrier to escape from a type I site, (T(H_I^{Close}, H_{IID}^{Far})), has gone from 0.47 to 0.10 eV close to the vacancy and the lowest energy site is not adjacent to the vacancy but further out as shown in Fig. 5.2. While the site of lowest energy is still on a type I oxygen, the raising of the energy for the corresponding site by the vacancy shows that in fact an oxygen vacancy by the dopant destabilizes the dopant trap.

TABLE 5.2: The relative energies of the initial site (i), transition state (TS), and final site (f) are shown for rotation (R), intra-octahedral transfer (T), and inter-octahedral transfer (I) in eV starting from the site closest to the vacancy in the yttrium system and the corresponding sites in the other systems. A * indicates the trigonal bipyramidal distortion in Al system. A - is used when this distortion leads to a transition being ill defined. A ° is used when only NEB and not cNEB was used for the TS.

Move(i,f)	**Sc** i	TS	F	**Y** i	TS	f
R(H_I^{Far}, H_I^{Far})	0.26	0.32	0.01	0.17	0.18	0.12
R(H_I^{Far}, H_I^{Close})	0.26	0.26	0.03	0.17	0.19	0.14
T(H_I^{Far}, H_{IID}^{Close})	0.26	0.36	0.36	0.17	0.17	0.07
R(H_I^{Close}, H_I^{Close})	0.25	0.25	0.04	0.10	0.25	0.22
R(H_I^{Close}, H_I^{Far})	0.25	0.25	0.04	0.10	0.17	0.17
T(H_I^{Close}, H_{IID}^{Far})	0.25	0.35	0.34	0.10	0.10	0.01
I(H_I^{Close}, H_{IID}^{Close})	0.25	0.56	0.54	0.10	0.22	0.22
R(H_{III}^{Far}, H_{III}^{Far})	0.35	0.46	0.30	0.36	0.36	0.31
T(H_{III}^{Far},H_{IIND}^{Close})	0.35	0.44	0.44	0.36	0.41	0.27
R(H_{III}^{Far}, H_{III}^{Close})	0.35	0.41	0.39	0.36	0.41	0.41
T(H_{III}^{Far}, H_{III}^{Close})	0.35	0.37	0.36	0.36	0.39	0.39
R(H_{III}^{Close}, H_{III}^{Close})	0.36	0.41	0.41	0.39	0.41	0.41
R(H_{III}^{Close}, H_{III}^{Far})	0.36	0.41	0.41	0.39	0.39	0.34
T(H_{III}^{Close}, H_{III}^{Far})	0.36	0.37	0.35	0.39	0.39	0.36
T(H_{III}^{Close},H_{IIND}^{Far})	0.36	0.43	0.41	0.39	0.40	0.24
I(H_{III}^{Close},H_{IIND}^{Close})	0.36	0.47	0.44	0.39	0.39	0.27
R(H_{IIND}^{Far},H_{IID}^{Close})	0.41	0.76	0.72	0.24	0.54	0.21
R(H_{IIND}^{Far},H_{IID}^{Far})	0.41	0.54	0.54	0.24	0.33	0.33
T(H_{IIND}^{Far}),H_{IIND}^{Close})	0.41	0.45	0.44	0.24	0.27	0.27
T(H_{IIND}^{Far},H_{III}^{Close})	0.41	0.43	0.36	0.24	0.40	0.39
R(H_{IIND}^{Close}, H_{IID}^{Far})	0.44	0.55	0.54	0.27	0.32	0.31
R(H_{IIND}^{Close}, H_{IID}^{Close}	0.44	0.77	0.71	0.27	0.47	0.47
T(H_{IIND}^{Close}),H_{IIND}^{Far})	0.44	0.45	0.41	0.27	0.27	0.24
T(H_{IIND}^{Close},H_{III}^{Far})	0.44	0.44	0.35	0.27	0.41	0.36
I(H_{IIND}^{Close},H_{III}^{Close})	0.44	0.47	0.36	0.27	0.39	0.39
T(H_{IID}^{Far}, H_{IID}^{Close})	0.54	0.62	0.37	0.32	0.32	0.06
R(H_{IID}^{Far},H_{IIND}^{Far})	0.54	0.55	0.41	0.32	0.32	0.26
R(H_{IID}^{Far},H_{IIND}^{Close})	0.54	0.55	0.44	0.32	0.32	0.27
R(H_{IID}^{Close},H_{IIND}^{Close})	0.54	0.54	0.49	0.21	0.37	0.34
I(H_{IID}^{Close},H_I^{Close})	0.54	0.56	0.24	0.21	0.33	0.09
T(H_{IID}^{Close}, H_{IID}^{Far})	0.54	0.63	0.33	0.21	0.21	0.0
R(H_{IID}^{Close},H_{IIND}^{Far})	0.54	0.54	0.46	0.22	0.32	0.31

5.3 Trajectory limiting barrier using Kinetic Monte Carlo

The kinetic monte carlo used in this study removed proton at one end of the box and reinserted back at the other end to prevent back and forth motion. The protons highlighted in Fig.5.5 are the ones that are removed from the upper boundary of the periodic box and reinserted back at the lower boundary of the periodic box.

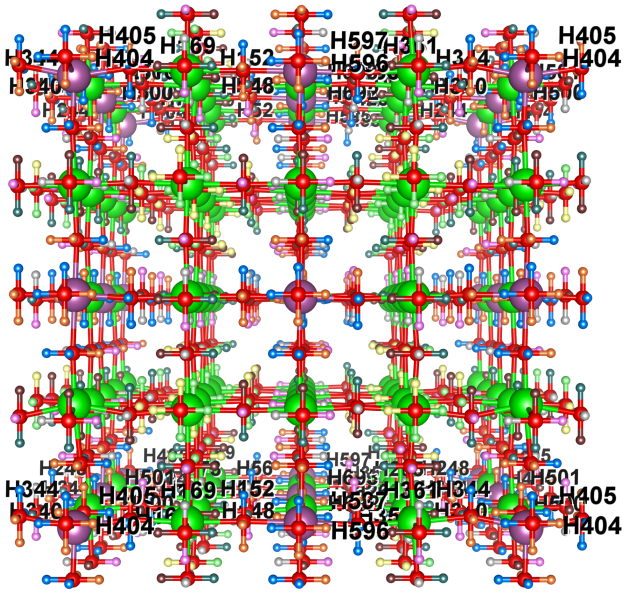

FIGURE 5.5: The protons that are removed from one end of the periodic box and reinserted back at the other end are highlighted.

Table 5.3 shows the percentage of limiting barrier move type found by KMC. The smallest Al system, all move appears at intra-octahedral transition which aligns with earlier findings[11]. However, for the largest Y system, the most abundant

type of limiting barrier now resides in rotational with 94 percent. The medium-sized Sc system, has 77 percent rotation and 23 percent intra-octahedral transition.

TABLE 5.3: The trajectory limiting barrier average is calculated by KMC and the percentage of each move type are recorded, with R representing rotation, T representing Intra-octahedral transition, and I representing inter-octahedral transition

Dopant	R	T	I
Al	0.00	1.00	0.00
Sc	0.77	0.23	0.00
Y	0.94	0.06	0.00

Chapter 6

Conclusions and future directions

This study aims to better understand the effect of scandium dopant on proton conduction in $BaZrO_3$, focusing on lattice structure, octahedral tilting, oxygen vacancy conduction, and proton trajectory. At the beginning, to prevent periodicity from magnifying the distortion created by the vacancy, this study expands the former $2 \times 2 \times 2$ system in each direction to obtain a $4 \times 4 \times 4$ system. In the expanded $4 \times 4 \times 4$ system, the lowest energy structure is found to be (-,-,-), which aligns with former results for Y doped $BaZrO_3$[10].

Both the distortion introduced by dopant and oxygen vacancy enhance the proton conduction landscape. Before the introduction of oxygen vacancy, data analysis of dopant's influence on optimum tilting and lattice size suggests that as dopant ionic size increase, both lattice size and octahedral tilting increase, as shown in Table 3.1 that the smallest dopant aluminum has the smallest lattice size; while the biggest dopant yittrium has the largest lattice size. Moreover, octahedral tilting measures based on comparison between Zr-O-Dopant angle and Zr-O-Zr angle in

Sc, Al and Y system show an increasingly shift away from 180 (linear) as dopant size increase, which aligns with the observed nonlinear Zr-O-Y arrangement in Giannici et al.[26].

After oxygen vacancy is introduced at the three possible distinct oxygen ion sites (nearest, second nearest and thir nearest), the local octahedral tilting induced by dopant are altered; thereby, leading to broadening of ZrOX angle, and the difference in relative energy between systems with distinct oxygen vacancy. For all systems, the lowest relative energy always appear at a dopant nearest neighbor oxygen site due to attraction between positive and negative defects. Measures of Boltzmann distribution further identify the nearest oxygen site as the region of highest probability. For Sc system, the nearest neighbor oxygen site is the most likely (nearly 100%) position for an oxygen vacancy; while for the Y system, the probability for the nearest oxygen sites is only twice the amount of the probability for the second nearest site.

Data analysis of relative energy as a function of proton distance away from oxygen vacancy for each proton category shows that the likelihood of proton conduction in Sc system is pretty high. In Fig.5.2, there are significant fluctuations and intersection between different proton sites at distances closer to the vacancy, suggesting proton conduction can take place. Also, as suggested by former study [10], proton conduction for small dopant system does not have inter-transition in the case without oxygen vacancy. Therefore, for the Sc case, there is no inter-octahedral

transition that travel toward the opposite proton directly, but two consecutive intra-octahedral transition.

Additionally, proton conduction in Sc system exhibit very similar pattern as Y system. Previous study of proton conduction in Al and Y show a huge difference towards trapping behavior. In Al system, protons are trapped near the dopant with some rare exceptions of escaping to non-dopant planes and perform long-range conduction; while in Y system, protons are kept by the dopant and perform long-range conduction in the same plane as dopant. Our result shows that unlike proton conduction in Al system that moved through proton binding sites on type I, II, and III oxygen ions, conduction in the Sc and Y system travel only through proton sites on type I and II oxygen ions as visualized in Fig.5.3, thereby, agreeing with previous study[11]. Our results also agrees with those of Kim etal who found that the dopant-vacancy ($V_O^{\bullet\bullet}$-D) association in Y and Sc are not effective enough to suppress the formation of proton trap[4], thus it is likely for proton trap to appear in the two systems.

Proton conduction trajectory can be further explored using KMC to simulate the evolution of the system on the potential energy surface over a long time scale. Using KMC, the percentage of limiting barrier move type are obtained. For the smallest Al system, all move appears at intra-octahedral transition which aligns with earlier findings[11]. However, for the larger Y system, the most abundant type of limiting barrier is now rotational. Similarly, for Sc system, the most abundant type of limiting barrier is also rotation.

This study fills in the missing puzzle to understand the effect of dopant size on proton conduction, and provides a starting point for future extension of finding the oxygen vacancy transition trajectory for the three dopant systems based on relative energy and Boltzmann probability results. For Scandium systems, the vacancy motion of sites nearest to the dopant would need to be considered; while for the Yttrium system, both sites nearest and second nearest to the dopant would need to be considered.

Appendix A

Appendix

A.0.1 Initial Glazer table

The initial relative energies for the 23 Glazer structures, optimized using VASP. The notation +/-/0 is used to describe tilting, according to the Glazer's notation, where + refers to subsequent layers tilting in the same directions, - in opposite directions, and 0 to no tilt [6].

A.0.2 KMC Code to generate initial file

KMC code is used to generate the initial file Energy.TS for the 4x4x4 system without oxygen vacancy. There are four column in the output file: the first and second column specify the initial and final proton number, the third column shows the type of proton transition, with 1 representing rotation, 2 representing intra-octahedral transfer, and 3 representing inter-octahedral transfer.

TABLE A.1: The relative energies for the 23 Glazer structures, optimized using VASP. The notation +/-/0 is used to describe tilting, as shown in trigonal bipyramidal distortion shown in Fig. 1.2.

Structure	Initial VASP structure	Energy(eV)	Relative Energy(eV)	frequency
1	(-,-,-)	-325.32	0.02	45.2
2	(+,+,+)	-325.31	0.03	36.5
3	(+,+,+)	-325.31	0.03	38.7
4	(-,+,-)	-325.34	0.00	23.4
5	(+,+,-)	-325.33	0.01	22.5
6	(-,+,-)	-325.34	0.00	25.4
7	(+,+,-)	-325.32	0.02	20
8	(+,+,-)	-325.33	0.01	18.8
9	(+,+,-)	-325.32	0.02	22.1
10	(+,-,-)	-325.34	0.00	26.6
11	(-,-,-)	-325.34	0.00	26.4
12	(-,-,-)	-325.32	0.02	18.1
13	(-,-,-)	-325.34	0.00	21.5
14	(-,-,-)	-325.32	0.02	23.6
15	(-,-,+)	-325.31	0.03	40.5
16	(-,-,-)	-325.31	0.03	40.9
17	(+,+,-)	-325.33	0.01	10.8
18	(+,+,-)	-325.33	0.01	27.5
19	(+,-,-)	-325.33	0.01	22.4
20	(-,-,-)	-325.33	0.01	25.7
21	(+,-,-)	-325.32	0.02	112.8
22	(+,+,-)	-325.34	0.00	115.1
23	(0,0,0)	-325.33	0.01	143.8

```
#!/usr/bin/env python

# making vesta category files

"""

"""


__copyright__ = "GPL"

__license__ = "Python"


import os

import time

import sys
```

```
import re
import numpy
from numpy import *
import operator


def periodic(arg1,arg2):
        #returns periodic difference
      dx=arg2-arg1
      while (dx<-0.5):
                  dx=dx+1.0
      while (dx>0.5):
                  dx=dx-1.0
      return dx



nOctants=8
nFirstOctant=12
ndim=nFirstOctant*nOctants
nTypes=8
Protons=numpy.zeros((nTypes,ndim),dtype=numpy.int)
indx=0
nH =0
counter=0
counterBackbone=0
lattice=numpy.zeros((3,3))
initialBackbonePositions=numpy.zeros((320,3))
HPos=numpy.zeros((769,3))


for line in open("AllProtonsAndBackBone.vasp"):
        if counter==1:
                dummy=line.split()
                size=eval(dummy[0])
        if counter>1 and counter <5:
                dummy=line.split()
                lattice[counter-2][0]=eval(dummy[0])
                lattice[counter-2][1]=eval(dummy[1])
```

```
                lattice[counter-2][2]=eval(dummy[2])
        if counter>7 and counter<328:
                dummy=line.split()
                initialBackbonePositions[counterBackbone][0]=eval(dummy[0])
                initialBackbonePositions[counterBackbone][1]=eval(dummy[1])
                initialBackbonePositions[counterBackbone][2]=eval(dummy[2])
                counterBackbone=counterBackbone+1
        if counter>=328:
                dummy=line.split()
                HPos[nH][0]=eval(dummy[0])
                HPos[nH][1]=eval(dummy[1])
                HPos[nH][2]=eval(dummy[2])
                nH=nH+1
        counter=counter+1

print "counter is "+str(counter)
print "counterBackbone is "+str(counterBackbone)
print "nH is "+str(nH)



#getting all proton to proton distances


distances=numpy.zeros((nH,nH))
for n in range(0,nH):
        for m in range(n+1,nH):
                dx=periodic(HPos[n][0],HPos[m][0])
                dy=periodic(HPos[n][1],HPos[m][1])
                dz=periodic(HPos[n][2],HPos[m][2])
                dxC=lattice[0][0] * dx + lattice[1][0] * dy + lattice[2][0] * dz
                dyC=lattice[0][1] * dx + lattice[1][1] * dy + lattice[2][1] * dz
                dzC=lattice[0][2] * dx + lattice[1][2] * dy + lattice[2][2] * dz
                distances[n][m]=size*((dxC ** (2)) + (dyC ** (2)) + (dzC ** (2))) ** (0.5)
                distances[m][n]=distances[n][m]
                #print n,m,distances[m][n]


#storing grouping information
```

```
listLabel=["TwiceRemovedO_OHpointsCloseO","TwiceRemovedO_OHpointsFarO","AdjacentO_OHpointsCloseO
,"OnceRemovedO_NoDopantFace_OHpointsCloseO","OnceRemovedO_NoDopantFace_OHpointsFarO"]

#Reading in proton number, relative energies,and grouping (0,...7)
colorType=numpy.zeros(769,int)
DistanceToVO=numpy.zeros(769)
Energies=numpy.zeros(769)
for n in range(0,769):
        Energies[n]=100.0
        colorType[n]=8

nColor=0
for groupName in listLabel:
  filename=groupName + ".in"
  for line in open(filename):
        dummy=line.split()
        which=eval(dummy[0])
        Energies[which-1]=eval(dummy[1])
        #DistanceToVO[which-1]=eval(dummy[3])
        #colorType[which-1]=nColor
  nColor=nColor+1

listLabel.append("notRun")

allTS = []

for n in range(0,nH):
        for m in range(n+1,nH):
                if distances[n][m]<2.5:
                        allTS.append([n+1, m+1, float(int(100.*distances[n][m]))/100.,Energies[n

print "AllTransition,should be 1728"
"""
for item in allTS:
        if item[3]!=100.0 and item[4]!=100.0:
                P1=item[0]
```

```
                P2=item[1]
                dP1P2=item[2]
                print P1,P2,dP1P2
"""
#reading a file to populate arrays
for line in open("ProtonTypes.dat"):
        dummy=line.split()
        for i in range(0,nFirstOctant):
                Protons[indx][i]=eval(dummy[i]);
        indx=indx+1

if (indx!=nTypes):
        print "indx is != nTypes\n"
        exit()

#Fill out the rest of the array
for indx in range(0,nTypes):
  for i in range(0,nFirstOctant):
      for j in range(1,nOctants):
              Protons[indx][i+nFirstOctant*j]=Protons[indx][i]+96*j

colors=["yellow","green","blue","orange","teal","brown","pink","gray"]
yellow= Protons[0]
green = Protons[1]
blue = Protons[2]
orange = Protons[3]
teal = Protons[4]
brown = Protons[5]
pink = Protons[6]
gray = Protons[7]
value = []
#print "yellow",yellow,"green",green,"blue",blue,"orange",\\
orange,"teal", teal,"brown", brown,"gray", gray,"pink", pink
#Rot_same_oxygen

for item in allTS:
```

```
 if item[2]<2:
  if item[0] in orange and item[1] in orange:
    print item[0],item[1],1,0.16
  if item[0] in blue and item[1] in blue:
    print item[0],item[1],1,0.06
  if item[0] in green and item[1] in green:
    print item[0],item[1],1,0.31
  if item[0] in yellow and item[1] in yellow:
    print item[0],item[1],1,0.25
  if item[0] in gray and item[1] in teal:
    print item[0],item[1],1,0.38
  if item[0] in teal and item[1] in gray:
    print item[0],item[1],1,0.38
  if item[0] in gray and item[1] in brown:
    print item[0],item[1],1,0.33
  if item[0] in brown and item[1] in gray:
    print item[0],item[1],1,0.33
  if item[0] in pink and item[1] in brown:
    print item[0],item[1],1,0.36
  if item[0] in brown and item[1] in pink:
    print item[0],item[1],1,0.36
  if item[0] in pink and item[1] in teal:
    print item[0],item[1],1,0.38
  if item[0] in teal and item[1] in pink:
    print item[0],item[1],1,0.38
  if item[0] in orange and item[1] in blue and item[2]<1.4:
    print item[0],item[1],1,0.05
  if item[0] in blue and item[1] in orange and item[2]<1.4:
    print item[0],item[1],1,0.05
  if item[0] in yellow and item[1] in green and item[2]<1.4:
    print item[0],item[1],1,0.25
  if item[0] in green and item[1] in yellow and item[2]<1.4:
    print item[0],item[1],1,0.25
#IntraT119_120is special case
for item in allTS:
 if item[2]<1.95:
```

```
  if item[0] in orange and item[1] in teal:
    print item[0],item[1],2,0.53
  if item[0] in teal and item[1] in orange:
    print item[0],item[1],2,0.53
  if item[0] in blue and item[1] in brown:
    print item[0],item[1],2,0.52
  if item[0] in brown and item[1] in blue:
    print item[0],item[1],2,0.52
  if item[0] in brown and item[1] in teal:
    print item[0],item[1],2,0.39
  if item[0] in teal and item[1] in brown:
    print item[0],item[1],2,0.39
  if item[0] in green and item[1] in pink:
    print item[0],item[1],2,0.37
  if item[0] in pink and item[1] in green:
    print item[0],item[1],2,0.37
  if item[0] in yellow and item[1] in gray:
    print item[0],item[1],2,0.36
  if item[0] in gray and item[1] in yellow:
    print item[0],item[1],2,0.36
  if item[0] in gray and item[1] in pink:
    print item[0],item[1],2,0.60
  if item[0] in pink and item[1] in gray:
    print item[0],item[1],2,0.60
  if item[0] in orange and item[1] in blue and item[2]>1.4:
    print item[0],item[1],2,0.05
  if item[0] in blue and item[1] in orange and item[2]>1.4:
    print item[0],item[1],2,0.05
  if item[0] in yellow and item[1] in green and item[2]>1.4:
    print item[0],item[1],2,0.47
  if item[0] in green and item[1] in yellow and item[2]>1.4:
    print item[0],item[1],2,0.47
#print "TwiceRemovedO_OHpointsCloseO\n",colors[0],Protons[0]
\end{center}
```

Listing A.1: KMC code

Bibliography

[1] K. D. Kreuer. Proton-conducting oxides. *Annu. Rev. Mater. Res.*, 33:333–359, 2003.

[2] M. A. Gomez, M. Chunduru, L. Chigweshe, L. Foster, S. J. Fensin, K. M. Fletcher, and L. E. Fernandez. The effect of yttrium dopant on the proton conduction pathways of $bazro_3$, a cubic perovskite. *Journal of Chemical Physics*, 132:214709, 2010.

[3] R. B. Cervera, Y. Oyama, S. Miyoshi, K. Kobayashi, T. Yagi, and S. Yamaguchi. Structural study and proton transport of bulk nanograined y-doped $bazro_3$ oxide protonics materials. *Solid State Ionics*, 179:236, 2008.

[4] H. S. Kim, A. Jang, S. Y. Choi, W. Jung, and S. Y. Chung. Vacancy-induced electronic structure variation of acceptors and correlation with proton conduction in perovskite oxides. *Angew Chem Int Ed Engl*, 55(43):13499–13503, 2016. doi: 10.1002/anie.201603835.

[5] G. Kresse and J. Furthmüller. Efficient iterative schemes for *ab initio* total-energy calculations using a plane-wave basis set. *Phys. Rev. B*, 54:11169–11186, Oct 1996. doi: 10.1103/PhysRevB.54.11169.

[6] A. M. Glazer. The classification of tilted octahedra in perovskites. *Acta Crystallographica, Section B: Structural Science*, 28:3384, 1972.

[7] A. Bilić and J. D. Gale. Ground state structure of $bazro_3$: A comparative first-principles study. *Physical Review B*, 79:174107, 2009.

[8] Rinlee Butch Cervera, Yukiko Oyama, Shogo Miyoshi, Itaru Oikawa, Hitoshi Takamura, and Shu Yamaguchi. Nanograined sc-doped bazro3 as a proton conducting solid electrolyte for intermediate temperature solid oxide fuel cells (it-sofcs). *Solid State Ionics*, 264:1–6, 2014. ISSN 01672738. doi: 10.1016/j.ssi.2014.06.010.

[9] M. A. Gomez, D. Shepardson, L. T. Nguyen, and T. Kehinde. Periodic long range proton conduction pathways in pseudo-cubic and orthorhombic perovskites. *Solid State Ionics*, 213:8–13, 2011.

[10] M. A. Gomez and F.-J. Liu. Protons in al doped $bazro_3$ escape dopant traps to access long range proton conduction highways. *Solid State Ionics*, 252: 40–47, 2013.

[11] RA Krueger, FG Haibach, DL Fry, and MA Gomez. Centrality measures highlight proton traps and access points to proton highways in kinetic monte carlo trajectories. *Journal of Chemical Physics*, 142:154110, 2015.

[12] John P. Arnold Sebastian Eisele Steffen Grieshammer Shu Yamaguchi Fabian M. Draber, Christiane Ader and Manfred Martin. Publisher correction: Nanoscale percolation in doped bazro3 for high proton mobility. *Nature Materials*, 2020. doi: 10.1038/s41563-020-0654-3.

[13] Maria A. Gomez, Gillian Kwan, Wanshu Zhu, Monica Chelliah, Xintong Zuo, Audrey Eshun, Virginia Blackmer, Truc Huynh, and Mai Huynh. Ordered yttrium concentration effects on barium zirconate structure, proton binding sites and transition states. *Solid State Ionics*, 304:126–134, 2017. ISSN 01672738. doi: 10.1016/j.ssi.2017.03.027.

[14] M. E. Björketun, Per G. Sundell, and G. Wahnström. *Physical Review B*, 76: 054307, 2007.

[15] G. Kresse and D. Joubert. From ultrasoft pseudopotentials to the projector augmented-wave method. *Phys. Rev. B*, 59:1758–1775, Jan 1999. doi: 10.1103/PhysRevB.59.1758. URL http://link.aps.org/doi/10.1103/PhysRevB.59.1758.

[16] G. Kresse. *Ab initio molekular dynamik für flüssige metalle*. PhD thesis, Technische Universität at Wien, 1993.

[17] G. Kresse and J. Hafner. Ab initio molecular-dynamics for liquid-metals. *Physical Review B*, 47:RC558, 1993.

[18] G. Kresse and J. Furthmüller. Efficiency of ab-initio total energy calculations for metals and semiconductors using a plane-wave basis set. *Computational Material Science*, 6:15–50, 1996.

[19] K. Burke. The abc of dft. 2007.

[20] P. Hohenberg and W. Kohn. Inhomogeneous electron gas. *Physical Review*, 136 (3B):B864B871, 1964.

[21] Levy Mel. Universal variational functionals of electron densities, first-order density matrices, and natural spin-orbitals and solution of the v-representability problem. *National Academy of Sciences*, 76 (12):60626065, 1979.

[22] G. Henkelman, B. P. Uberuaga, and H. Jonsson. A climbing image nudge elastic band method for finding saddle points and minimum energy paths. *J. Chem. Phys.*, 113:9901, 2000.

[23] G. Henkelman and H. Jonsson. Long time scale kinetic monte carlo simulations without lattice approximation and predefined event table. *Journal of Chemical Physics*, 115:9657–9666, 2001.

[24] http://theory.cm.utexas.edu/vtsttools/dynmat/.

[25] A. F. Voter. Introduction to the kinetic monte carlo method. In K. E. Sickafus and E. A. Kotomin, editors, *Radiation Effects in Solids*. Springer, NATO Publishing Unit, Dordrecht, The Netherlands, 2005.

[26] F. Giannici, M. Shirpour, A. Longo, A. Martorana, R. Merkle, and J. Maier. Long-range and short-range structure of proton-conducting y:bazro3. *Chemistry of Materials*, 23(11):2994–3002, 2011. ISSN 0897-4756. doi: 10.1021/cm200682d. URL <GotoISI>://WOS:000291294100041.

[27] K. D. Kreuer, S. Adams, W. Munch, A. Fuchs, U. Klock, and J. Maier. Proton conducting alkaline earth zirconates and titanates for high drain electrochemical applications. *Solid Sate Ionics*, 145:295, 2001.